INTERNATIONAL JOURNAL FOR NUMERICAL METHODS IN FLUIDS
Int. J. Numer. Meth. Fluids 2008; **57**:1459–1483
Published online 27 December 2007 in Wiley InterScience (www.interscience.wiley.com). DOI: 10.1002/fld.1656

Boussinesq cut-cell model for non-linear wave interaction with coastal structures

D. Z. Ning[1,2], J. Zang[3,*,†], Q. Liang[4], P. H. Taylor[2] and A. G. L. Borthwick[2]

[1]*State Key Laboratory of Coastal and Offshore Engineering, Dalian University of Technology, Dalian 116023, China*
[2]*Department of Engineering Science, Oxford University, Oxford OX1 3PJ, U.K.*
[3]*Department of Architecture and Civil Engineering, University of Bath, Bath BA2 7AY, U.K.*
[4]*School of Civil Engineering and Geosciences, Newcastle University, Newcastle NE1 7RU, U.K.*

SUMMARY

Boussinesq models describe the phase-resolved hydrodynamics of unbroken waves and wave-induced currents in shallow coastal waters. Many enhanced versions of the Boussinesq equations are available in the literature, aiming to improve the representation of linear dispersion and non-linearity. This paper describes the numerical solution of the extended Boussinesq equations derived by Madsen and Sørensen (*Coastal Eng.* 1992; **15**:371–388) on Cartesian cut-cell grids, the aim being to model non-linear wave interaction with coastal structures. An explicit second-order MUSCL-Hancock Godunov-type finite volume scheme is used to solve the non-linear and weakly dispersive Boussinesq-type equations. Interface fluxes are evaluated using an HLLC approximate Riemann solver. A ghost-cell immersed boundary method is used to update flow information in the smallest cut cells and overcome the time step restriction that would otherwise apply. The model is validated for solitary wave reflection from a vertical wall, diffraction of a solitary wave by a truncated barrier, and solitary wave scattering and diffraction from a vertical circular cylinder. In all cases, the model gives satisfactory predictions in comparison with the published analytical solutions and experimental measurements. Copyright © 2007 John Wiley & Sons, Ltd.

Received 25 June 2007; Revised 13 September 2007; Accepted 2 October 2007

KEY WORDS: Boussinesq equations; finite volume method; Cartesian cut cell; Godunov method; non-linear waves; coastal structures

*Correspondence to: Jun Zang, Department of Architecture and Civil Engineering, University of Bath, Bath BA2 7AY, U.K.
†E-mail: J.Zang@bath.co.uk

Contract/grant sponsor: U.K. Engineering and Physical Science Research Council; contract/grant numbers: GR/T07220/01, GR/T07220/02

1. INTRODUCTION

Many maritime structures, such as piers, jetties, and offshore wind turbine stacks, are composed of vertical surface-piercing cylinders situated in water of intermediate to shallow depth. The component cylinders are subject to inertia and drag loads arising from the instantaneous flow field, which is driven by waves and currents as they interact with the structure. Engineers are particularly interested in determining the flow field about vertical cylinders in extreme waves, which may arise from large-scale displacements as a series of solitary-like waves or as storm-driven wave groups. As waves approach the shore, they shoal, refract, break, and reflect. When encountering large structures, waves scatter and diffract. Although these transformation processes may be modelled in detail by solving the 3-D Reynolds-averaged Navier–Stokes (RANS) equations, the computational cost is beyond the capacity of present-day computers. A practical alternative for modelling non-breaking waves is to use the Boussinesq equations, which are essentially a depth-averaged model, and incorporate some of the features of vertical motions and thus include non-hydrostatic pressure effects. With recent improvements in the treatment of linear dispersion and non-linear characteristics [1–4], numerical models based on the Boussinesq-type equations are becoming widely used to provide an accurate description of coastal hydrodynamics. Boussinesq-type equations have been successfully solved by the finite difference method (FDM) [5–7], finite element method (FEM) [8–10], and finite volume method (FVM) [11–13].

In order to model the interaction of waves, currents and maritime structures using a Boussinesq-type equation solver, it is necessary to generate a suitable boundary conforming grid. This is of great importance in simulations where the near body hydrodynamics have to be correctly calculated in order to compute loadings. Of the various mesh generation techniques available, the Cartesian cut-cell approach pioneered by Causon and co-workers [14, 15] is particularly attractive in that it is easy to implement and gives an accurate representation of very complicated boundaries, while leaving the rest of the grid composed of cells whose faces are aligned parallel to Cartesian coordinate axes. The solid bodies are extracted from the underlying Cartesian grid with the solid–fluid boundaries approximated as piecewise linear segments. This method has been successfully applied in many fields including the Euler equations in 2D [16, 17] and 3D [18, 19], the shallow water equations [20, 21] and extended to deal with low-speed incompressible flows [22, 23] and flows involving moving material interfaces [24, 25].

This paper describes a Godunov-type finite-volume Cartesian cut-cell numerical scheme for solving the enhanced Boussinesq equations derived by Madsen and Sørensen [1]. The two-step MSCL-Hancock predictor–corrector method is used to achieve overall second-order accuracy. The model is used to simulate solitary wave reflection from a vertical wall and the diffraction of a solitary wave by a truncated barrier. Further simulations are presented for the interaction of a solitary wave with a surface-piercing cylinder. The results demonstrate that the present scheme is capable of solving Boussinesq-type equations for waves interacting with cylindrical maritime structures. The approach is easy to extend to coastal situations involving complicated boundaries.

2. GOVERNING EQUATIONS

The Boussinesq equations in terms of the depth-averaged velocity with improved dispersive characteristics derived by Madsen and Sørensen [1] may be expressed in differential conservative form

DOI: 10.1002/fld

using vector notation as

$$\mathbf{q}_t+\mathbf{f}_x+\mathbf{g}_y=\mathbf{s} \tag{1}$$

where subscripts x, y and t denote differentiation with respect to space and time, and $\mathbf{q}$, $\mathbf{f}$, $\mathbf{g}$ and $\mathbf{s}$ are vectors representing conserved variables, fluxes in the x- and y-directions, and source terms. Neglecting viscous fluxes and bed friction, the vectors are

$$\begin{aligned}
\mathbf{q}&=\begin{bmatrix}\eta\\ P\\ Q\end{bmatrix}=\begin{bmatrix}\eta\\ ud\\ vd\end{bmatrix},\quad \mathbf{f}=\begin{bmatrix}ud\\ u^2d+g(\eta^2+2\eta h)/2\\ uvd\end{bmatrix}\\
\mathbf{g}&=\begin{bmatrix}vd\\ uvd\\ v^2d+g(\eta^2+2\eta h)/2\end{bmatrix},\quad \mathbf{s}=\begin{bmatrix}0\\ g\eta h_x+\psi_x\\ g\eta h_y+\psi_y\end{bmatrix}
\end{aligned} \tag{2}$$

Here, η is the surface elevation above the still water level, h is still water depth, d is total water depth ($d=h+\eta$), u and v are the Cartesian depth-averaged velocity components, and ψ_x and ψ_y are the Boussinesq dispersive terms defined by

$$\begin{aligned}
\psi_x=&(B+\tfrac{1}{3})h^2(P_{xxt}+Q_{xyt})+Bgh^3(\eta_{xxx}+\eta_{xyy})\\
&+hh_x(\tfrac{1}{3}P_{xt}+\tfrac{1}{6}Q_{yt}+2Bgh\eta_{xx}+Bgh\eta_{yy})+hh_y(\tfrac{1}{6}Q_{xt}+Bgh\eta_{xy})
\end{aligned} \tag{3}$$

$$\begin{aligned}
\psi_y=&(B+\tfrac{1}{3})h^2(Q_{yyt}+P_{xyt})+Bgh^3(\eta_{yyy}+\eta_{xxy})\\
&+hh_y(\tfrac{1}{3}Q_{yt}+\tfrac{1}{6}P_{xt}+2Bgh\eta_{yy}+Bgh\eta_{xx})+hh_x(\tfrac{1}{6}P_{yt}+Bgh\eta_{xy})
\end{aligned} \tag{4}$$

where B is a dispersion coefficient and g is the acceleration due to gravity. Following Madsen and Sørensen [1], B is set to $\frac{1}{15}$ which best represents shallow water linear dispersion.

On the fixed body in the present model, the fully reflective slip boundary conditions are imposed and given by

$$\eta_{\mathrm{G}}=\eta_{\mathrm{I}},\quad \hat{u}_{\mathrm{G}}=-\hat{u}_{\mathrm{I}},\quad \hat{v}_{\mathrm{G}}=\hat{v}_{\mathrm{I}} \tag{5}$$

where the subscripts G and I represent ghost and inner boundary cells, respectively; $\hat{u}$ and $\hat{v}$ denote the velocity normal and tangential to the solid boundary. The reflective slip boundary conditions also translate into zero tangential velocity gradient and normal velocity component at a boundary point under consideration.

3. CARTESIAN CUT-CELL TECHNIQUE

In order to simulate flows around obstacles or within complicated domains, the grid should be boundary fitting. Simple approaches like the staircase fit obtained by employing a Cartesian grid

DOI: 10.1002/fld

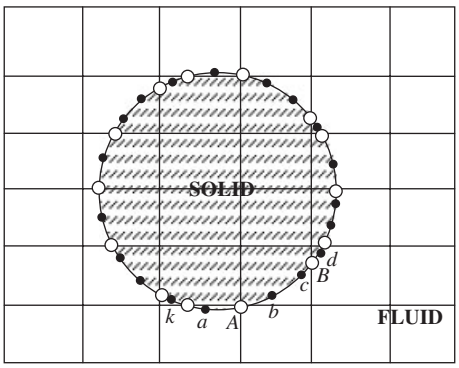

solid black dots—seeding points; white circle—intersections.

Figure 1. Intersection points between line segment and cell interfaces.

with boundaries approximated by straight-line segments aligned with the co-ordinate directions lead to spurious flow reflections and vorticity generation in the vicinity of the staircase—exactly where it is important to obtain an accurate flow field for force calculations. A large body of work has been undertaken into overcoming this problem through irregular star, curvilinear, unstructured triangular, and Cartesian cut-cell body-fitted grids [26–32]. Of these approaches, the Cartesian cut-cell technique is particularly attractive as it is straightforward and automatic to implement, permits the overall Cartesian mesh to retain its simple connectivity, and avoids the need to evaluate Jacobin metrics that introduce errors into curvilinear grid solutions, particularly for highly skewed cells. The generation of a Cartesian cut-cell grid essentially involves identifying internal, external, and boundary cells in a Cartesian grid (which may itself be uniform, nested, quadtree, etc.) and treating the boundary cells separately as multi-sided flow cells with one or more sides forming the boundary. Causon *et al.* [14, 15] provide a detailed description of the Cartesian cut-cell methodology.

In the present work, the cut cells are generated as follows. A background uniform Cartesian grid is created that covers the entire flow domain. Internal solid boundaries are identified using seeding points, which are ordered anticlockwise to form closed loops. Figure 1 shows an example of such a loop of internal boundary seeding points (the solid black dots) created about a circle. The grid cells containing seeding points are located by searching all the cells in the background grid.

An intersection between the line segment connecting two boundary seeding points and a cell interface occurs if two neighbouring seeding points are located in different cells. Consider the internal boundary seeding points in Figure 1, represented by solid black dots $(a, b, c, \ldots, k)$. The coordinates of the intersections where the body surface crosses the underlying grid are determined by linear interpolation and denoted by white circles in Figure 1. After all the intersections have been identified, they are joined to form cut cells, whose indices are flagged. Herein a cut cell refers to the polygon formed by the fluid part of the original cell and the cut edge (line segment connecting two intersections). Each cut-cell polygon can have from three to five faces and can be categorized into four types according to the angle (φ) formed by the cut edge and the x-axis. The cut-cell categories are $\varphi \in [0°, 90°)$, $\varphi \in [90°, 180°)$, $\varphi \in [180°, 270°)$, and $\varphi \in (270°, 360°)$. Each cut-cell category may be further classified into four sub-types. For example, Figure 2 illustrates

DOI: 10.1002/fld

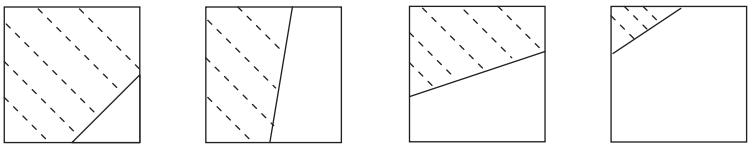

Figure 2. Grid generation: sub-type of cut cell for case with $\varphi \in [0°, 90°)$.

the four sub-types obtained for cut cells where $\varphi \in [0°, 90°)$. The sub-types for other cases can be obtained by rotation.

After all the cut cells have been produced, each cell in the grid is flagged, according to whether it is a fluid cell, cut cell, or a solid cell.

4. NUMERICAL MODEL

4.1. High-resolution FVM

By splitting the surface gradient terms using the balancing method of Rogers *et al.* [33] and transferring the temporal terms to the left-hand side of Equation (1), a deviatoric form of Madsen and Sørensen's [1] enhanced Boussinesq equation may be expressed in integral form within a cell-centred finite volume scheme as

$$\frac{\partial}{\partial t}\int_\Omega \mathbf{q}^* \,\mathrm{d}\Omega + \int_\Omega \left(\frac{\partial \mathbf{f}}{\partial x} + \frac{\partial \mathbf{g}}{\partial y}\right)\mathrm{d}\Omega = \int_\Omega \mathbf{s}^* \,\mathrm{d}\Omega \tag{6}$$

where the numerical domain is denoted by Ω and the vectors $\mathbf{q}^*$ and $\mathbf{s}^*$ are expressed as

$$\mathbf{q}^* = \begin{bmatrix} \eta \\ P^* \\ Q^* \end{bmatrix} = \begin{bmatrix} \eta \\ P - (B+\frac{1}{3})h^2(P_{xx}+Q_{xy}) - hh_x(\frac{1}{3}P_x + \frac{1}{6}Q_y) - \frac{1}{6}hh_yQ_x \\ Q - (B+\frac{1}{3})h^2(Q_{yy}+P_{xy}) - hh_y(\frac{1}{3}Q_y + \frac{1}{6}P_x) - \frac{1}{6}hh_xP_y \end{bmatrix} \tag{7}$$

and

$$\mathbf{s}^* = \begin{bmatrix} 0 \\ g\eta h_x + Bgh^3(\eta_{xxx}+\eta_{xyy}) + Bgh^2h_x(2\eta_{xx}+\eta_{yy}) + Bgh^2h_y\eta_{xy} \\ g\eta h_y + Bgh^3(\eta_{yyy}+\eta_{xxy}) + Bgh^2h_y(2\eta_{yy}+\eta_{xx}) + Bgh^2h_x\eta_{xy} \end{bmatrix} \tag{8}$$

Applying Green's theorem to the second term of Equation (6) gives

$$\frac{\partial}{\partial t}\int_\Omega \mathbf{q}^* \,\mathrm{d}\Omega + \oint_S \hat{\mathbf{f}}\,\mathrm{d}S = \int_\Omega \mathbf{s}^* \,\mathrm{d}\Omega \tag{9}$$

DOI: 10.1002/fld

where S is the interaction path of Ω and $\hat{\mathbf{f}}$ is the vector of the combined flux functions given by

$$\hat{\mathbf{f}} = \mathbf{f} n_x + \mathbf{g} n_y \tag{10}$$

with n_x and n_y being the x and y components of the outward pointing unit normal vector ($\mathbf{n}$) to S. Equation (6) is solved using a Godunov-type finite volume scheme with appropriate modifications for Cartesian cut-cell meshes. To maintain second-order accuracy, the two-step MUSCL-Hancock method [34] is employed. During the predictor half-time step $\Delta t/2$, a non-conservative approach is taken whereby the intermediate cell centre value is evaluated from

$$(A\mathbf{q}^*)_{i,j}^{n+1/2} = (A\mathbf{q}^*)_{i,j}^{n} - \frac{\Delta t}{2}\left(\sum_{k=1}^{m} \hat{\mathbf{f}}_k^n \cdot \mathbf{l}_k - (A\mathbf{s}^*)_{i,j}^{n}\right) \tag{11}$$

where A is the area of cell (i, j), superscript n denotes the time level, the vector $\mathbf{l}_k$ is the length of side k multiplied by $\mathbf{n}$, and m is the maximum number of cell sides. For a flow cell, $m=4$ and for a cut cell ranges from 3 to 5. $\hat{\mathbf{f}}_k^n$ is the flux vector through cell side k, evaluated from the flow variables at time level n. The calculation of the interface fluxes is performed within each cell using interpolated values at the central extremities of the inner interfaces. During the corrector step, the interface fluxes are calculated over the full-time step and the intermediate solution from the predictor step is used to solve a series of Riemann problems using the HLLC [35] approximate Riemann solver. The cell interface fluxes obtained from these Riemann problems are used to update the flow solution over the time interval Δt from

$$(A\mathbf{q}^*)_{i,j}^{n+1} = (A\mathbf{q}^*)_{i,j}^{n} - \Delta t\left(\sum_{k=1}^{m} \hat{\mathbf{f}}_k^{n+1/2} \cdot \mathbf{l}_k - (A\mathbf{s}^*)_{i,j}^{n+1/2}\right) \tag{12}$$

where $\hat{\mathbf{f}}_k^{n+1/2}$ is the flux vector through cell side k evaluated based on the flow variables resulting from the predictor step.

After obtaining the vector of intermediate variables $\mathbf{q}^*$, the linear system of equations formed by Equation (7) needs to be solved for the vector of conserved variables $\mathbf{q}$, which are discretized by central differences on a uniform, collocated grid. For example, the central difference expression for P is

$$\begin{aligned} P_{i,j}^* = P_{i,j} &- \left(B+\frac{1}{3}\right)h^2\left(\frac{P_{i+1,j}-2P_{i,j}+P_{i-1,j}}{\Delta x^2}+\frac{Q_{i+1,j+1}-Q_{i-1,j+1}-Q_{i+1,j-1}+Q_{i-1,j-1}}{4\Delta x\Delta y}\right) \\ &- h\frac{h_{i+1,j}-h_{i-1,j}}{2\Delta x}\left(\frac{1}{3}\frac{P_{i+1,j}-P_{i-1,j}}{2\Delta x}+\frac{1}{6}\frac{Q_{i,j+1}-Q_{i,j-1}}{2\Delta y}\right) \\ &- \frac{h}{6}\frac{h_{i,j+1}-h_{i,j-1}}{2\Delta y}\frac{Q_{i+1,j}-Q_{i-1,j}}{2\Delta x} \end{aligned} \tag{13}$$

in which Δx and Δy are the grid cell dimensions and the subscripts i and j are the Cartesian cell indices. The discretized form of Equation (7) is a linear system,

$$\mathbf{U}\mathbf{x} = \mathbf{b} \tag{14}$$

DOI: 10.1002/fld

in which **U** is a sparse and symmetric matrix whose coefficients are time independent and can be pre-computed for a fixed grid. The vectors **x** and **b** are

$$\mathbf{x}=\begin{pmatrix} P_{1,1} \\ Q_{1,1} \\ P_{2,1} \\ \vdots \\ P_{n,n} \\ Q_{n,n} \end{pmatrix} \quad \text{and} \quad \mathbf{b}=\begin{pmatrix} P^*_{1,1} \\ Q^*_{1,1} \\ P^*_{2,1} \\ \vdots \\ P^*_{n,n} \\ Q^*_{n,n} \end{pmatrix} \tag{15}$$

The linear system is positive definite and symmetric; hence, the unknown vector **x** is solved using the conjugate gradient method.

4.2. Stability criterion

The stability of the present scheme is constrained by the Courant–Friedrichs–Lewy (CFL) criterion, such that the time step employed is

$$\Delta t = C \min(\Delta t_x, \Delta t_y) \tag{16}$$

where

$$\Delta t_x = \min_i \frac{\Delta x_i}{|u_i| + \sqrt{g h_i}} \tag{17}$$

with an analogous definition for Δt_y. The Courant number C was taken to be 0.65 in our calculations, which is close to the stability bound. Subscript i is the cell index, and Δx_i is the cell size in the x direction.

4.3. Treatment of cut cells

The numerical solver is constructed on a Cartesian fluid cell template. Near the solid boundary, cut cells contain both fluid and solid faces and a single cell interface may have both fluid and solid parts. To implement the boundary conditions properly, each cut cell is first classified according to its size. A large cut cell is defined as having an area larger than or equal to half that of the host grid cell from which it is cut. When the area of a cut cell is smaller than half its host cell, such a cell is defined as being small.

When evaluating interface fluxes for a large cut cell, the flow data at the cell face are approximated using the following reconstruction procedure:

$$u(x, y) = u_{i,j} + \mathbf{r} \cdot \nabla \mathbf{u}^{\text{mod}}_{i,j} \tag{18}$$

where **r** is the normal distance vector from the cell centre to a specific point (x, y) on a cell interface which is defined to be positive in the east and north directions, $\nabla \mathbf{u}^{\text{mod}}_{i,j}$ is the limited gradient vector modified for calculating fluxes across the flow boundaries of any given large cut

DOI: 10.1002/fld

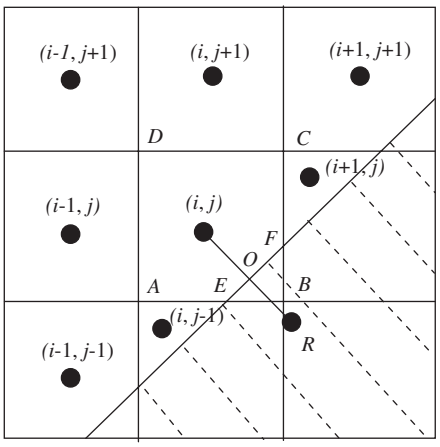

Figure 3. Calculation of cut-cell fluid and solid gradients.

cell. Following Yang *et al.* [17] and Causon *et al.* [14] and taking the x-direction gradient vector of cell (i, j) in Figure 3 as an example, the fluid and solid gradients can be expressed by

$$\nabla \mathbf{u}_{i,j}^{\mathrm{mod\,f}} = \Psi(l)\frac{u_{i,j}-u_{i-1,j}}{\Delta x_{i-1/2,j}} \quad \text{and} \quad \nabla \mathbf{u}_{i,j}^{\mathrm{mod\,s}} = \Psi(l)\frac{u_{i,j}-u_{i-1,j}}{\Delta x_{i-1/2,j}} \tag{19}$$

in which $\Psi(l)$ is a slope limiter, and $\Delta x_{i-1/2,j} = x_{i,j} - x_{i-1,j}$. The slope limiter is evaluated from [31]

$$\Psi(l) = \max[0, \min(\beta l, 1), \min(l, \beta)] \tag{20}$$

in which l is the ratio of successive gradients and β is the limiter parameter ($1 \leqslant \beta \leqslant 2$) (see e.g. Toro [35]). In the present work, the min–mod limiter $\beta = 1$ is used because of its superiority in terms of numerical stability. For fluid gradients, the ratio of successive gradients is given by

$$l = \frac{(q_{i+1,j}-q_{i,j})/\Delta x_{i+1/2,j}}{(q_{i,j}-q_{i-1,j})/\Delta x_{i-1/2,j}} \tag{21}$$

where q represents one of the principal flow variables, η, (P) and (Q), and $\Delta x_{i+1/2,j} = x_{i+1,j} - x_{i,j}$. For solid gradients, the ratio is defined as

$$l = \frac{(q_R-q_{i,j})/\Delta x_{i,R}}{(q_{i,j}-q_{i-1,j})/\Delta x_{i-1/2,j}} \tag{22}$$

in which $\Delta x_{i,R} = x_R - x_{i,j}$. Flow information for the fictional cell R is obtained using linear interpolation based on values at cell (i, j) and at the boundary point O. If cell face DA separates both fluid and solid parts, the calculation is similar, with vector $(u_{i,j}-u_R)/\Delta x_{i,R}$ taking the place of the corresponding term in Equation (19) when evaluating solid gradients, and $\Delta x_{i,R} = x_{i,j} - x_R$. The x-direction limited gradient vector for the large cut cell (i, j) is given by

$$\nabla \mathbf{u}_{i,j}^{\mathrm{mod}} = \frac{\nabla y_{\mathrm{s}} \nabla \mathbf{u}_{i,j}^{\mathrm{mod\,s}} + \nabla y_{\mathrm{f}} \nabla \mathbf{u}_{i,j}^{\mathrm{mod\,f}}}{\nabla y} \tag{23}$$

DOI: 10.1002/fld

where $\nabla y_s = |BF|$, $\nabla y_f = |FC|$, $\nabla y = |BC|$. Now $\nabla y = \nabla y_s + \nabla y_f$, so Equation (23) includes the cases with $\nabla y_s = 0$ or $\nabla y_f = 0$, in which the modified limited gradient vector $\nabla u_{i,j}^{\text{mod}}$ simply reduces to either the fluid or solid gradient term. The above formula can be extended to the y-direction in a similar manner. Once all the face values of the conservative flow variables are obtained, the interface fluxes through cell faces *AE*, *FC*, *CD* and *DA* are evaluated using the corresponding formulations for the predictor and corrector steps.

The fluxes through the cut edge (*EF* in Figure 3) must also be properly evaluated in order to maintain the conservation properties of the numerical scheme. However, the normal velocity component on the cut edge *EF* is zero for slip (reflective) boundary conditions. Therefore, there is no convective flux through the cut edge. The only component of the inviscid fluxes through the cut edge is $g(\eta + 2\eta h_s)/2$.

Using Cartesian cut cells to approximate curved boundaries, very small cut cells are often generated. In an explicit numerical scheme, these small cells lead to the requirement of a very small time step to avoid numerical instability. A conventional means of overcoming this computationally inefficient requirement is to merge the small cells with a neighbouring larger cell. However, the increased cell sizes near the boundary may reduce the solution accuracy. Hence, we use the ghost-cell immersed boundary method (GCIBM) proposed by Tseng and Ferziger [36] to treat the small cut cells. The flow information at the small cut cells is interpolated from the boundary conditions and neighbouring cells as explained by Liang *et al.* [20].

In the present study, it should be stressed that the Boussinesq terms in Equations (3) and (4) are simply omitted from the cut cells, so that locally the equations reduce to the non-linear shallow water equations. Careful testing shows that this does not appear to affect the results, as the short wave dispersive Boussinesq effects are negligible in the very small region containing cut cells at the fluid domain boundary. Thus, the complex mixed spatial and temporal derivatives in the Boussinesq terms are accurately treated as source terms within the solver over the bulk of the domain, where the grid geometry is simple Cartesian, and a simple test is used to turn off these terms for the cut cells.

5. RESULTS

Three test cases are considered: solitary wave reflection from a solid wall; diffraction from a truncated thin wall; and a wave scattering and diffraction from a vertical surface-piercing circular cylinder in a wave tank. In each case, second-order solitary wave elevation and flux components in the x- and y-directions are provided at the input boundary. The results presented here satisfy previous grid convergence tests.

5.1. Solitary wave reflection from a vertical wall

The first validation test concerns solitary wave reflection from a vertical wall in a horizontal-bottomed straight flume with still water depth of 1 m, for which second-order analytical solutions and experimental measurements are available. The computational domain is 20 m long by 0.04 m wide, and discretized spatially with 1000×2 cells. In one grid configuration, a 0.03 m thick wall occupying $1\frac{1}{2}$ cells is situated at the right-hand end of the domain (Figure 4(a)). Simulations are carried out for solitary waves of varying wave height H initially introduced 10 m from the wall, and the computations terminated before the reflected wave from the wall reaches the left boundary.

DOI: 10.1002/fld

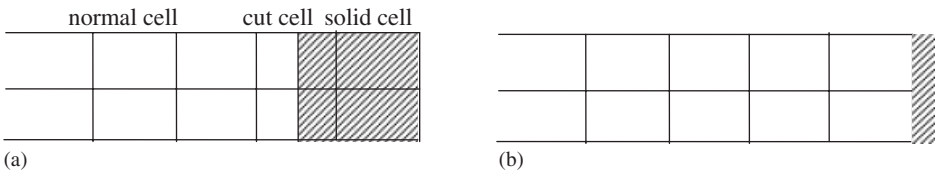

Figure 4. Grid cells near the vertical wall: (a) cut cells and (b) total reflection.

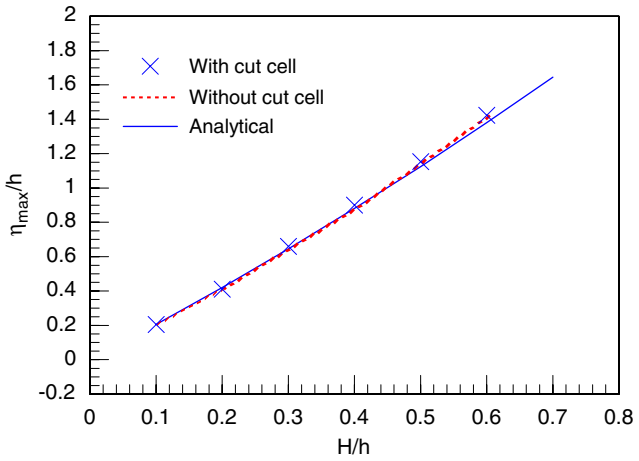

Figure 5. Maximum run up at vertical wall for varying H.

For comparison purposes, similar computations have been carried out with a second grid configuration whereby right-hand wall is replaced by a fully reflective boundary without cut cells as depicted in Figure 4(b). Figure 5 shows the agreement obtained between the predicted maximum run up at the wall (obtained with and without cut cells) and the second-order analytical solution of Byatt-Smith [37] derived from the non-linear superposition of two waves moving in opposite directions, as

$$\frac{\eta_{\max}}{h} = 2\frac{H}{h} + \frac{1}{2}\left(\frac{H}{h}\right)^2 \tag{24}$$

Figure 6 shows the time t_0, at which maximum run up occurs as a function of increasing wave height H. As expected, the taller solitary waves move faster. Figure 7 shows the computed solitary wave profiles along the flume at different times $t = t_0, t_0 \pm 0.8, t_0 \pm 1.6$, and $t_0 \pm 2.4$ s for waves of non-dimensional heights $H/h = 0.1$ and 0.6, respectively. The reflected wave profiles barely alter after reflection regardless of whether the incoming solitary wave has small (a) or large (b) amplitude. This test confirms that the cut cells have been implemented properly for normally incident wave reflection and that the scheme is accurate at phase-resolution.

5.2. Diffraction of a solitary wave by a truncated wall

The second validation test examines the diffraction of a solitary wave by a thin surface-piercing vertical wall that extends about two-thirds the way across a wave tank. Figure 8 provides a plan

DOI: 10.1002/fld

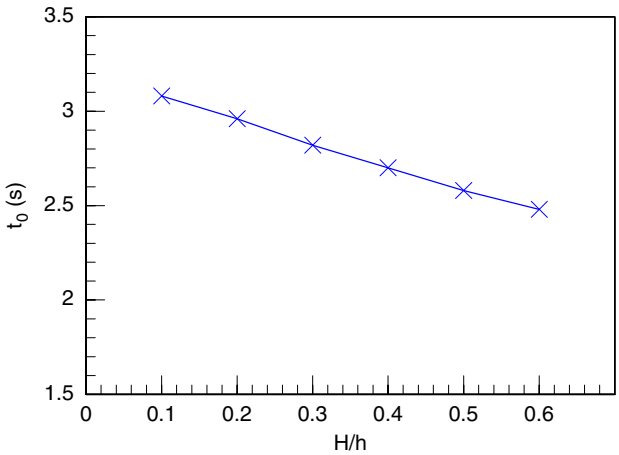

Figure 6. Occurrence time of maximum run up for varying H.

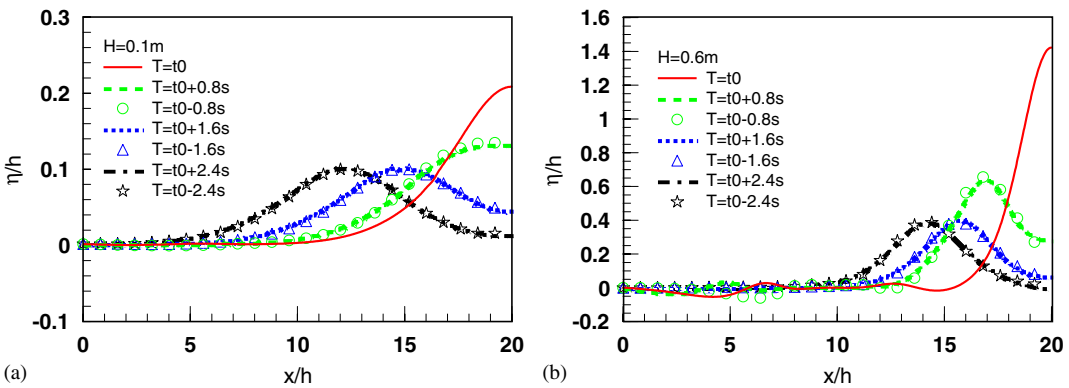

Figure 7. Solitary wave profiles along the flume at different times.

view of the portion of the flume near the wall, corresponding to the layout of the flume used by Perroud [38], who obtained experimental measurements of the incident and diffracted wave field due to solitary wave interaction with the barrier. The solid wall is 0.008 m wide, the gap between the truncated end of the wall at A and the flume side wall W2 is 0.508 m. The still water depth is 0.061 m. Perroud [38] carried out a parameter study by varying the ratio of the incident solitary wave height to water depth H/h. Water elevation measurements were made using wave gauges at locations, expressed (later) in polar coordinates (r, θ) from the origin O at the trailing corner of the truncated wall indicated in Figure 8. The computational domain is 1.6 m long $\times$ 1.6 m wide and discretised with a uniform grid of 400×400 cells. The initial crest position of the solitary wave is 0.48 m upwave from the truncated barrier. The Cartesian coordinates of two corners of the barrier are A (0.68 m, 0.508 m) and O (0.688 m, 0.508 m) where the origin is at the south-west corner of the tank.

DOI: 10.1002/fld

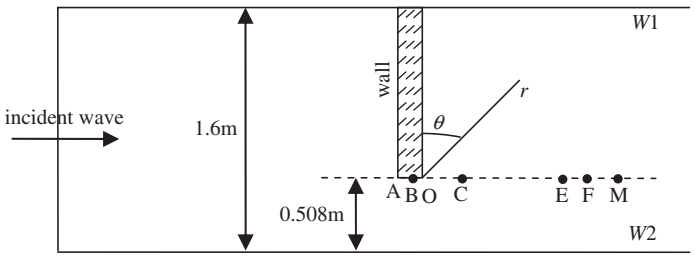

Figure 8. Definition sketch of truncated wall in flume.

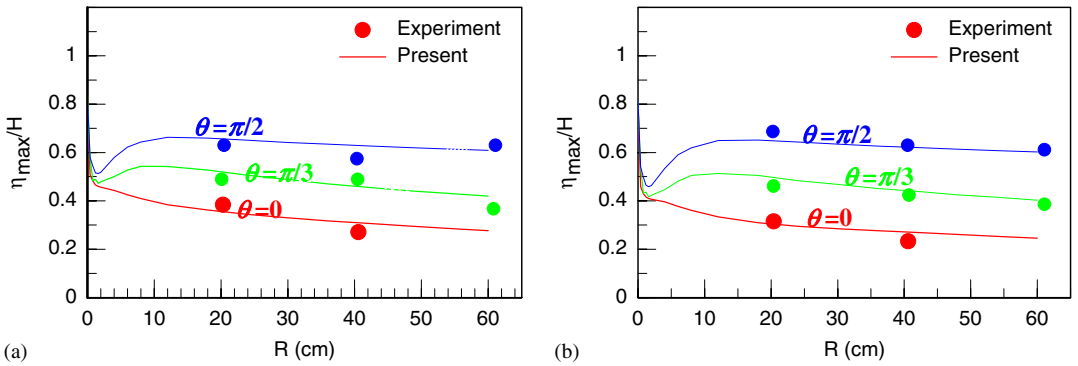

Figure 9. Predicted and measured [38] diffraction coefficients for different H/h: (a) $H/h=0.27$ and (b) $H/h=0.42$.

Figure 9 shows the agreement between the predicted and measured diffraction coefficients for two solitary waves with wave height to depth ratios of 0.27 and 0.42, respectively. The ratio of the diffracted wave height to the incident wave height ($\eta_{\max}/H$) is plotted against radial distance r for different θ. In the lee of the wall, the maximum wave elevation varies with distance from the tip of the truncated wall as follows. Close to the tip of the truncated wall at $r\sim 1$ cm, the non-dimensional maximum wave elevation reduces to a value between 0.4 and 0.5. Along the $\theta=0$ line which is immediately behind the wall, the non-dimensional wave elevation reduces asymptotically to a value of about 0.2 as wave energy leaks into the shadow region behind the wall. Along the $\theta=\pi/2$ line, the non-dimensional maximum wave elevation recovers to a value between 0.6 and 0.7 at $r\sim 14$ cm, then decreases asymptotically towards about 0.6.

Figure 10 presents the predicted wave elevation time histories along the $\theta=\pi/2$ line at B, O, C, E, F and M at $r=-0.4, 0, 0.4, 29.6, 30$ and 30.4 cm, respectively, for $H/h=0.42$. The wave elevation time histories vary with spatial distance in the region near the tip of the truncated wall change even though the spacing between B, O and C is Δx (Figure 10(a)). Far from the truncated wall, the time histories are almost identical (Figure 10(b)).

Figure 11 depicts the non-dimensional maximum run up profile along the front face of the truncated wall (from the tip A to the lateral sidewall W1). Diffraction effects are most evident within 30 cm of the tip A. Near W1, the maximum run up (and hence reflection coefficient) becomes

DOI: 10.1002/fld

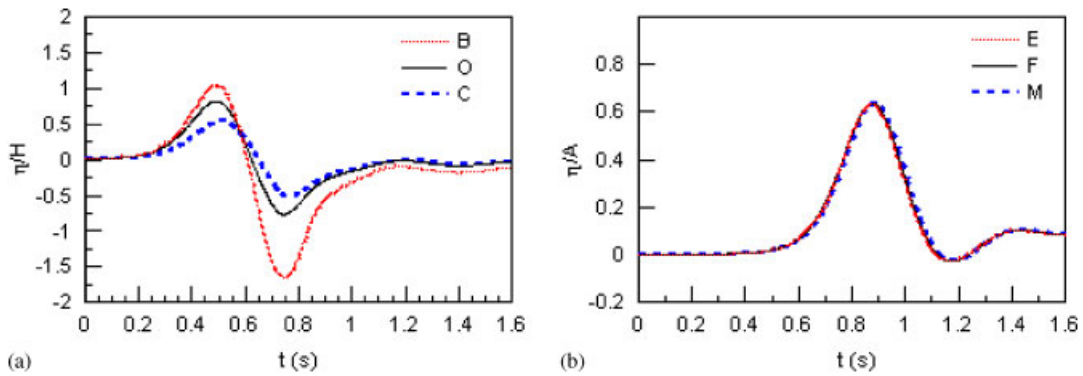

Figure 10. Wave elevation time histories at different locations along the $\theta=\pi/2$ line for $H/h=0.42$: (a) near wall: B, O, C and (b) far from wall: E, F, M.

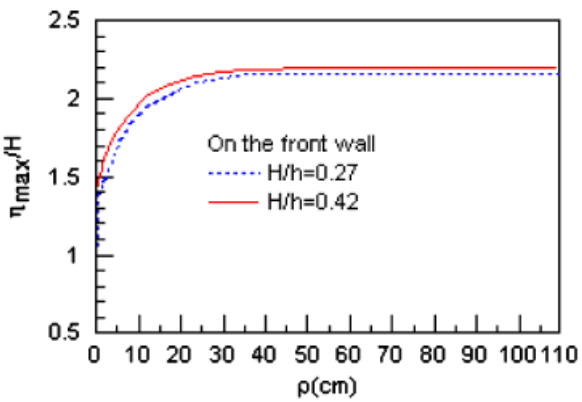

Figure 11. Variation of wave crest with different distance from point a on the front wall.

almost constant at about 2.16 and 2.2 which are almost identical to the Byatt-Smith analytical results from Equation (24) of $\eta/H=2.21$ for $H/h=0.42$ and 2.14 for $H/h=0.27$, respectively.

Figure 12 illustrates the diffraction process after the incident solitary wave interacts with the truncated wall by means of a time sequence of 3-D plots of the surface elevation and the corresponding contours, when $H/h=0.42$. The solitary wave reaches the truncated wall at $t\sim0.32$ s (Figure 12(a)). Water then rises up the front face of the wall, and the wave begins to reflect. Diffraction effects commence from the tip of the wall. At $t\sim0.57$ s, the maximum run up has occurred at the front face of the wall. Meanwhile, diffracted waves start to enter the otherwise still water in the lee of the truncated wall (Figure 12(b)). By $t=0.77$ s, the solitary wave has split into a forward diffracted wave and a back-scattered reflected wave (Figure 12(c)). Secondary back-scattered and forward-scattered waves begin to emanate outward from the tip of the wall and respectively follow the leading reflected and diffracted waves. A vortex develops at the tip of the wall. Figure 12(d) shows the situation at $t=1.02$ s.

DOI: 10.1002/fld

5.3. Solitary wave diffraction from a vertical surface-piercing circular cylinder

In order to test the ability of the present numerical model to resolve solitary wave interaction with a typical configuration for an offshore wind turbine foundation, we consider the scattering and diffraction of a solitary wave after it meets a vertical surface-piercing circular cylinder. The case

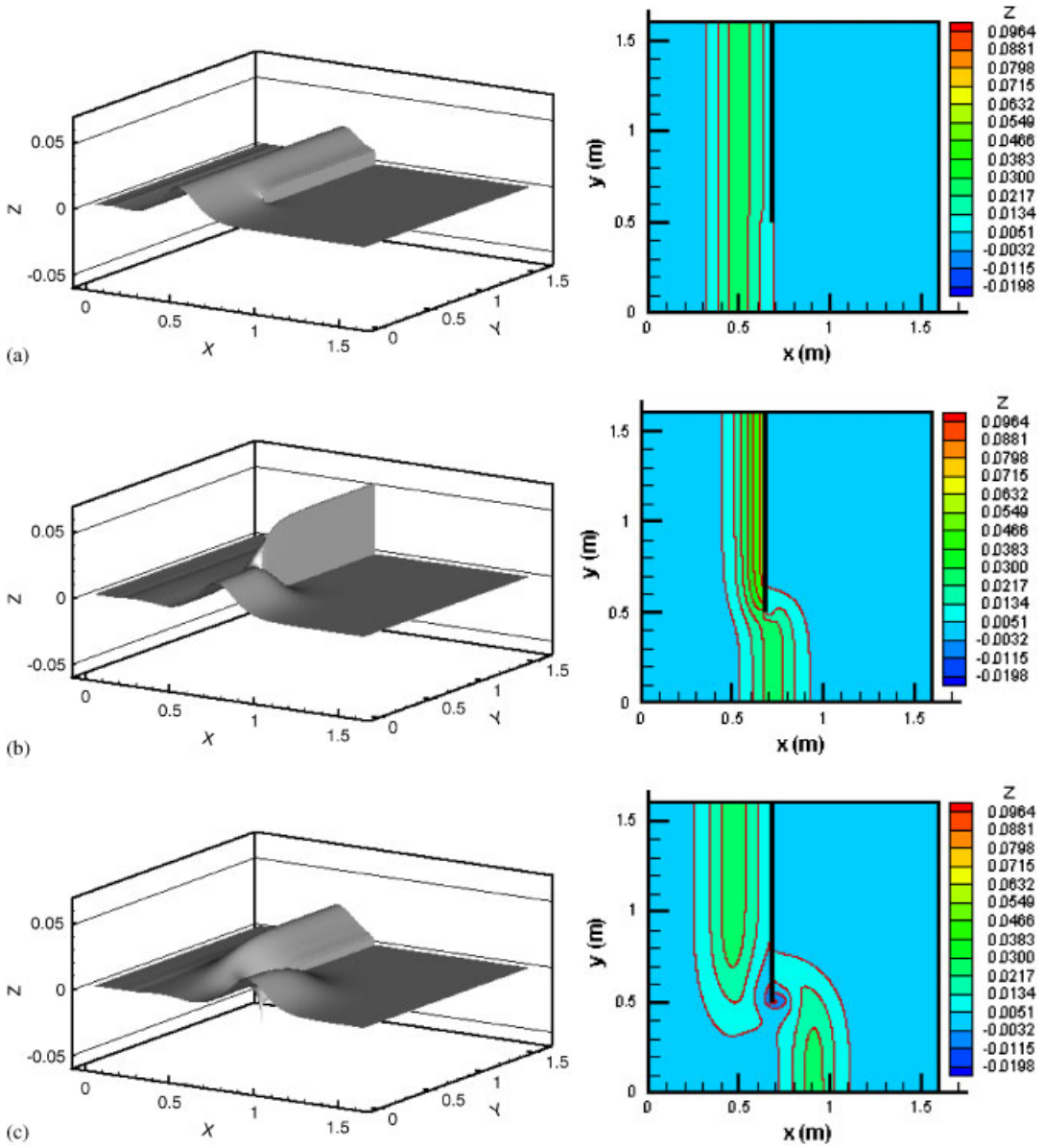

Figure 12. Wave diffraction at a truncated wall: 3-D view of wave profiles and free surface contours at different times: (a) $t = 0.32$ s; (b) $t = 0.57$ s; (c) $t = 0.77$ s; and (d) $t = 1.02$ s.

DOI: 10.1002/fld

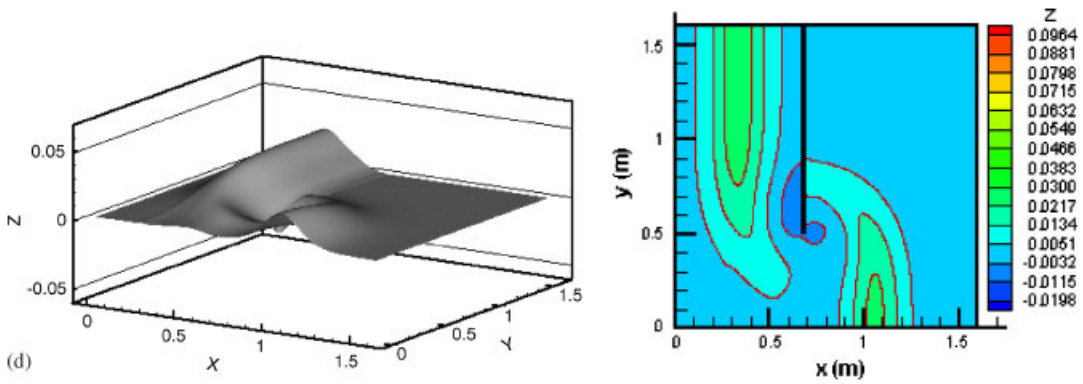

Figure 12. *Continued*.

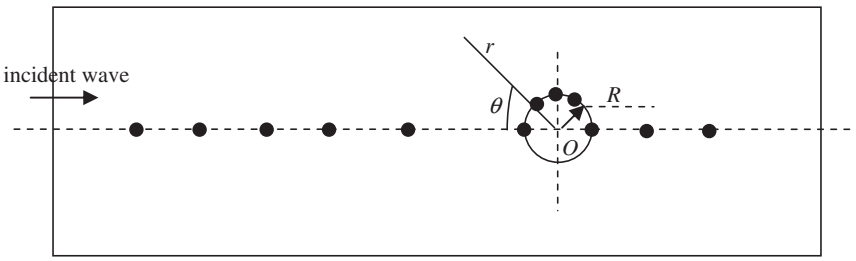

Figure 13. Definition sketch: solitary wave interaction with a circular cylinder.

is identical to that studied experimentally by Yates and Wang [39] in a horizontal-bottomed wave tank 7.6 m long and 0.76 m wide in which the still water depth is $h=4$ cm. A vertical cylinder of radius $R=6.35$ cm is located on the longitudinal centreline of the channel. The incoming solitary wave is of height 1.6 cm such that $\eta_{\text{incident}}/h=0.4$. The computational domain is of length 3 m and width 0.76 m and is discretized by a 750×190 Cartesian grid. The central axis of the cylinder is located at O (2.0 m, 0.38 m), where the coordinates have their origin at the south-west corner of the tank. The initial maximum solitary wave profile is generated at 1.0 m from the western boundary of the domain (Figure 13).

Figure 14 shows the cut cell and equivalent staircase Cartesian grids that are generated in the vicinity of the circular cylinder. It is obvious that the cut-cell grid provides a much smoother boundary representation than the staircase.

Figures 15–18 compare the predicted and measured time histories of the dimensionless surface elevation at four gauges along the radial lines $\theta=0, 60, 120$ and 180° (where θ is measured clockwise from the x-axis through the centre of the cylinder, such that the $\theta=0$ and 180° lines are taken westward and eastward along the longitudinal centreline of the tank, as indicated in Figure 13). Alternative numerical results obtained by Yates and Wang [39] using an FEM solver are also plotted. In the figures, the time axis of the numerical predictions has been shifted so that the peak wave amplitudes coincide with the experimental data. In general, the present numerical predictions agree well with the measured and alternative numerical data. Both numerical models

DOI: 10.1002/fld

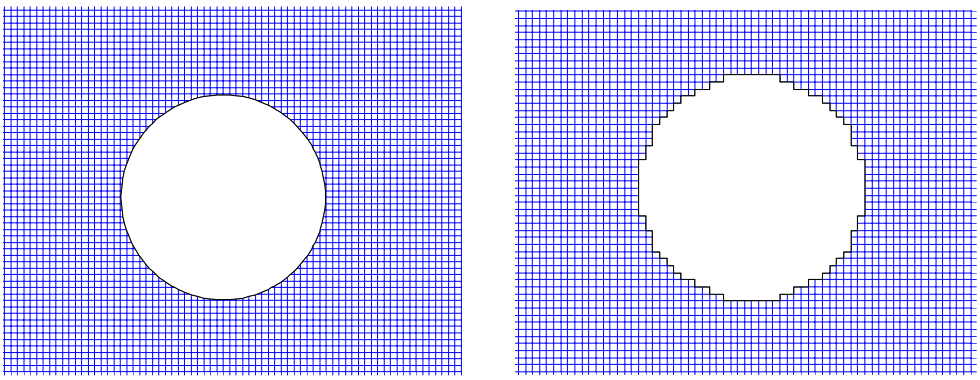

Figure 14. Cartesian grids surrounding the circular cylinder with two methods: (a) present (cut cell) and (b) traditional (staircase).

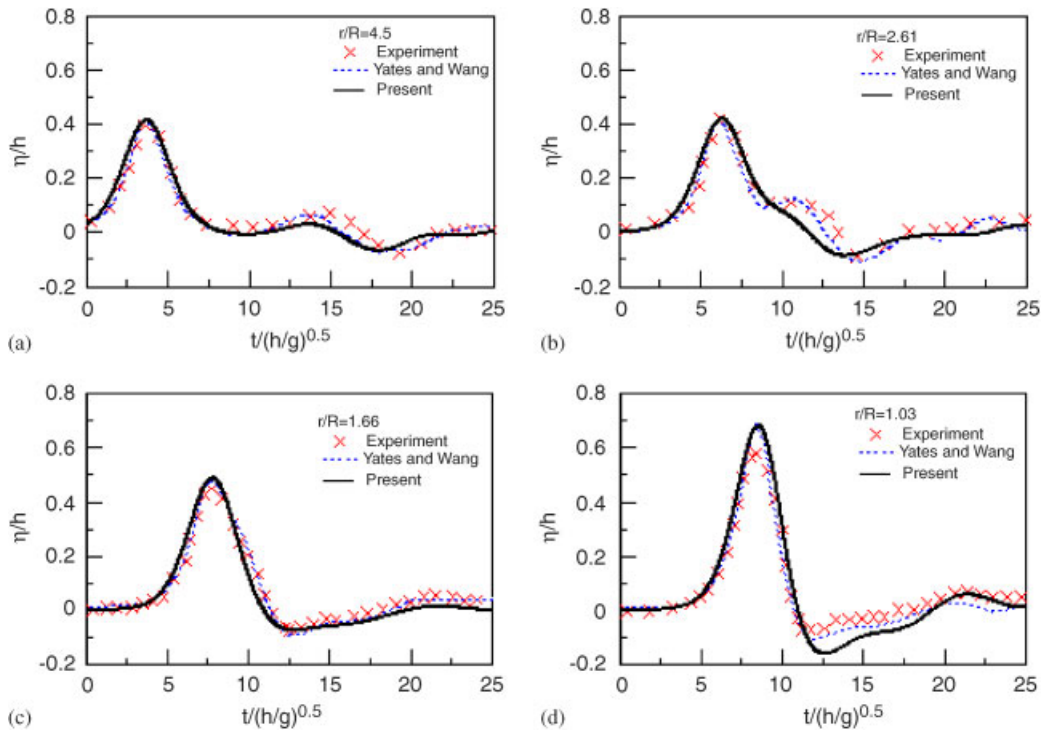

Figure 15. Time history of free surface elevation along $\theta = 0°$.

overestimate the maximum run up very close to the cylinder (at $r/R = 1.03$ in Figures 15(d), 17(d) and 18(d), where r is the radial distance from the centre of the cylinder) mainly due to the omission of viscosity and surface tension in the simulation. The non-dimensional free surface

DOI: 10.1002/fld

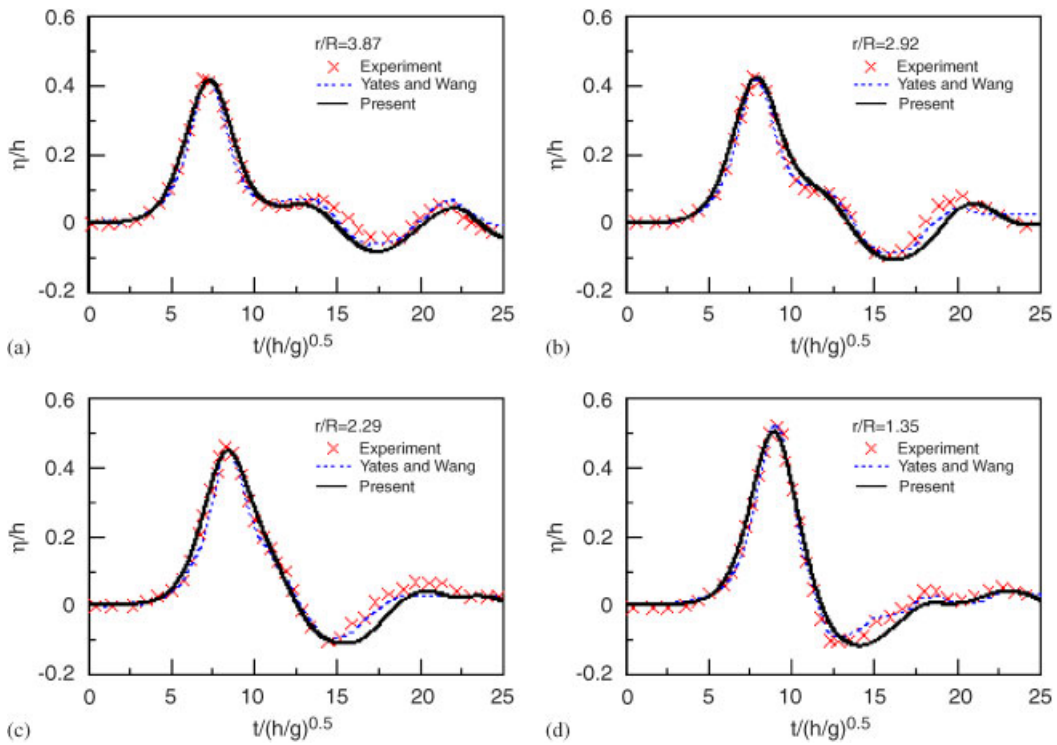

Figure 16. Time history of free surface elevation along $\theta = 60°$.

elevation time histories in Figures 15(a), 16(a), (b), 17(a) and (b) have secondary peaks due to the scattered waves. Along the radial line $\theta = 0°$, the peak wave surface elevation increases in magnitude towards the cylinder (Figure 15).

Overall the comparisons between the numerical simulations and the experimental data downstream of the cylinder are good. At $r/R = 1.35$ (i.e. 2 cm downstream), there is no sign of viscous wake effects. As before, at $r/R = 1.03$, the predicted peak free surface elevations are higher than measured. Figure 19 shows the free surface profiles along the centreline of the wave tank at different times. This depicts the solitary wave approaching, interacting with and passing the cylinder. Peak run up occurs at $t = 1.28$ s.

To visualize the scattering process, Figure 20 contains 3-D views of the water surface and free surface elevation contours at $t = 0.08$, 1.28 and 1.68 s, which correspond to the early propagation of the solitary wave before it reaches the cylinder, the solitary wave interacting with the cylinder at the instant of maximum run up, and the scattered and diffracted field after the solitary wave has passed the cylinder.

By subtraction of the incident solitary wave from the complete diffraction solution, details of the scattered wave are obtained (Figure 21). The scattered wave structure is relatively simple early in the interaction, with the water surface raised on the upstream side of the cylinder and weakly depressed behind. After the reflected scattered wave moves upstream away from the cylinder, the water surface drops significantly at the front of the cylinder as well as in its lee. At $t \sim 1.80$ s,

DOI: 10.1002/fld

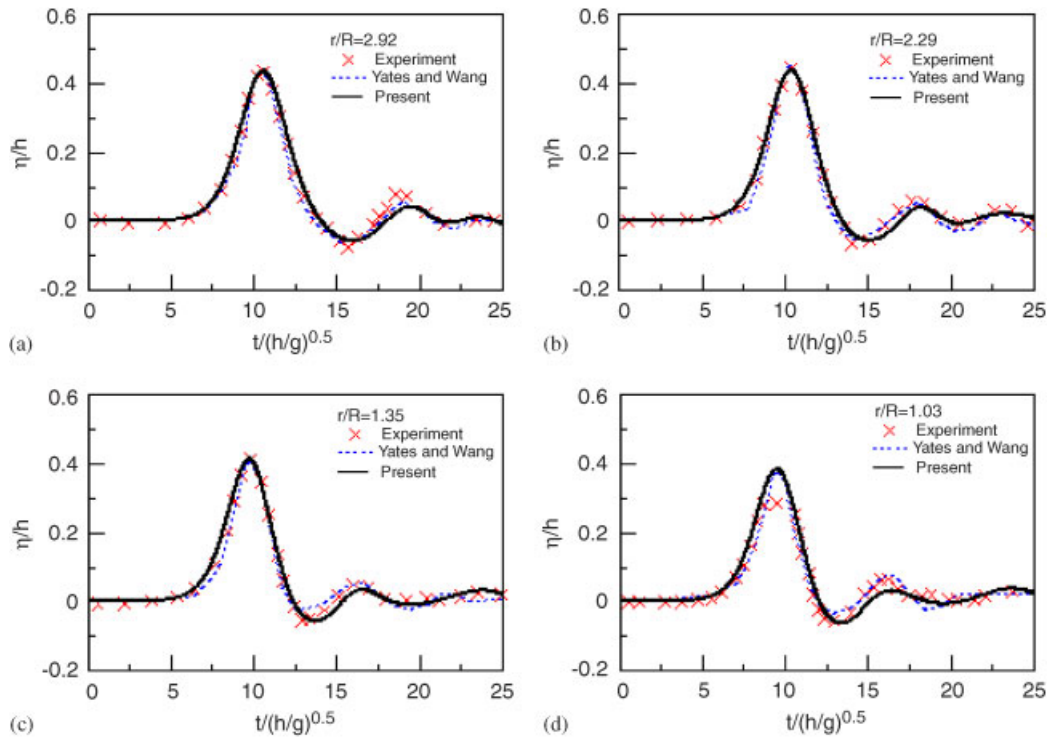

Figure 17. Time history of free surface elevation along $\theta = 100°$.

a characteristic three peaked ring wave can be seen moving outwards: one of the peaks travels along the centreline and the others are orientated at about $\pm 45°$ to the downstream direction. This three-peaked ring structure is very similar to that observed by Buldakov *et al.* [40, 41] in their work on the diffraction of compact wave groups by a cylinder. Buldakov *et al.* report that the structure is due to the second-order sum contribution to the scattered field. The complicated spatial distribution of the peaks in Figure 21 is related to the propagation and collision of short wave disturbances around the body surface. It is encouraging and perhaps surprising that the present Boussinesq-type model can reveal such detailed local structure.

Figure 22 compares the wave elevations for the cut-cell and staircase Cartesian grid methods at $r/R = 2.92$ and 1.36. As would be expected, the difference between the two sets of results is large close to the cylinder especially at the peak time, but decays away from the cylinder. The cut-cell technique is much better than the staircase grid in locally resolving wave interactions with complicated structural elements.

These results demonstrate that the present cut-cell Boussinesq model is able to simulate strongly non-linear waves interacting with cylindrical structures. Further computations have been carried out to study the effects of water depth h and wave height H on wave run up. Here, the centre of the cylinder is taken as the origin of the coordinates and the rectangular computational domain is defined as $(-15R \leqslant x \leqslant 15R) \times (-7R \leqslant y \leqslant 7R)$. Figure 23 shows the maximum non-dimensional wave elevations occurring at any time along the centreline and around the surface of the cylinder

DOI: 10.1002/fld

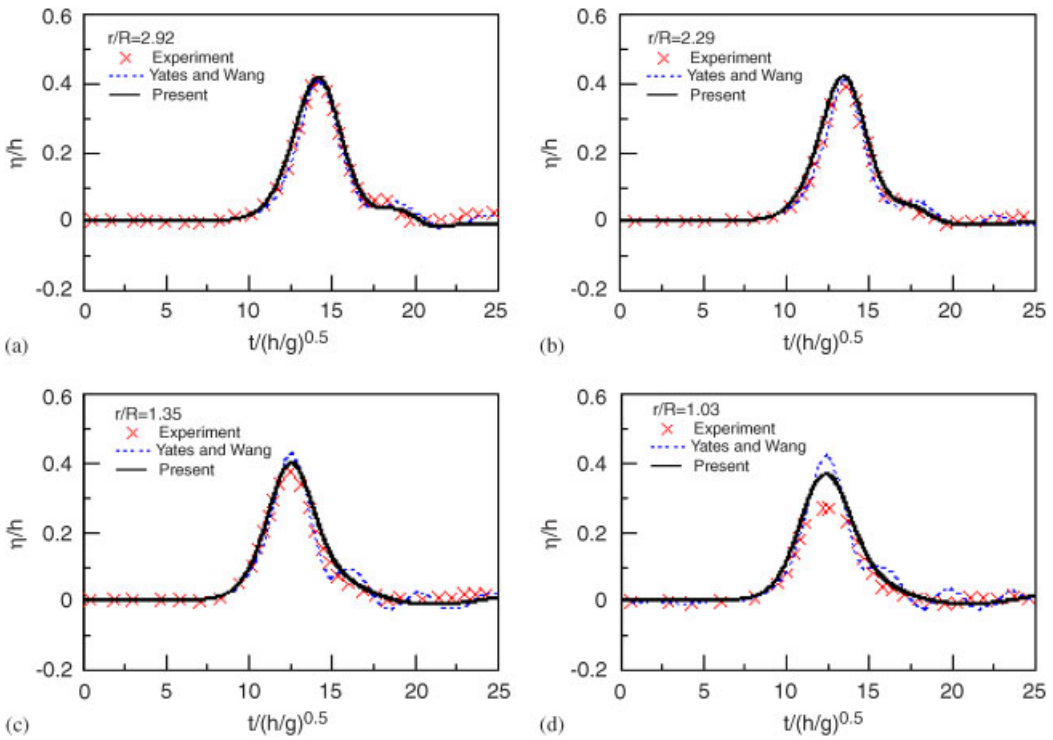

Figure 18. Time history of free surface elevation along $\theta = 180°$.

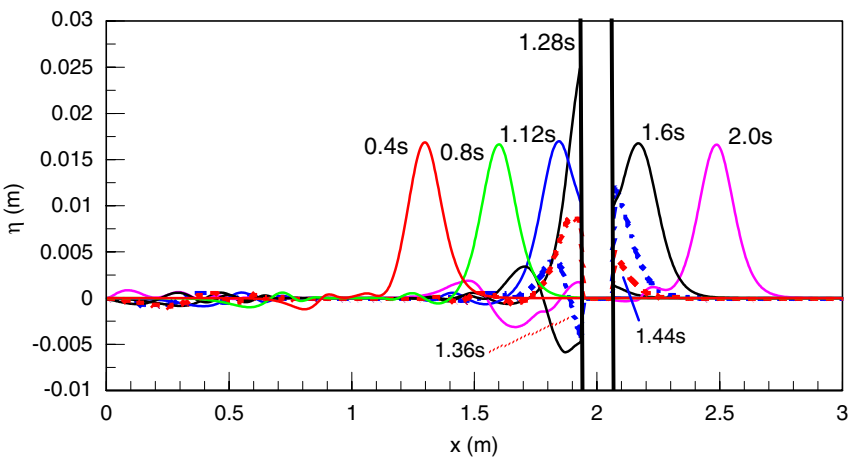

Figure 19. Wave profile along the centreline at different times.

DOI: 10.1002/fld

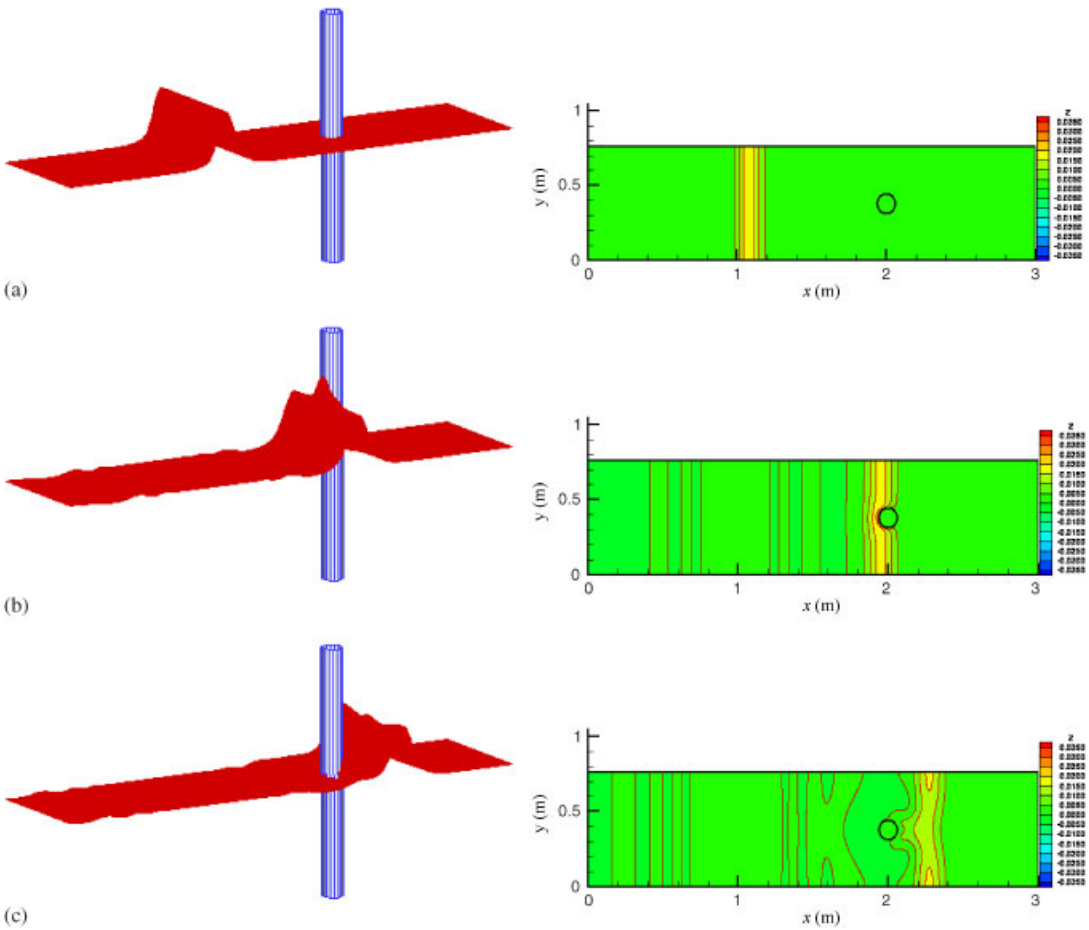

Figure 20. 3-D view of wave profile and the corresponding contours at different times: (a) $t=0.08$ s; (b) $t=1.28$ s; and (c) $t=1.68$ s.

for undisturbed water depth $h/R=1.0$ and 2.0 with different wave heights ($H/h=0.1, 0.2, 0.4$). For steeper non-linear solitary waves, the maximum surface elevation always occurs at the front stagnation point. The lowest maximum elevation occurs slightly to the rear of the shoulder of the cylinder, close to the point when the maximum Bernoulli suction occurs, and this point moves farther round the cylinder towards the rear stagnation point as the degree of non-linearity is increased.

Figure 24 shows the maximum non-dimensional wave elevations along the centreline for non-dimensional wave heights $H/h=0.1$ and 0.2 for different ratios of still water depth to cylinder radius ($h/R=1.0, 2.0, 3.0$), respectively. The crest and trough of a bow-like wave occur close to the front and rear of the cylinder, whose magnitude increases as the relative depth shallows.

DOI: 10.1002/fld

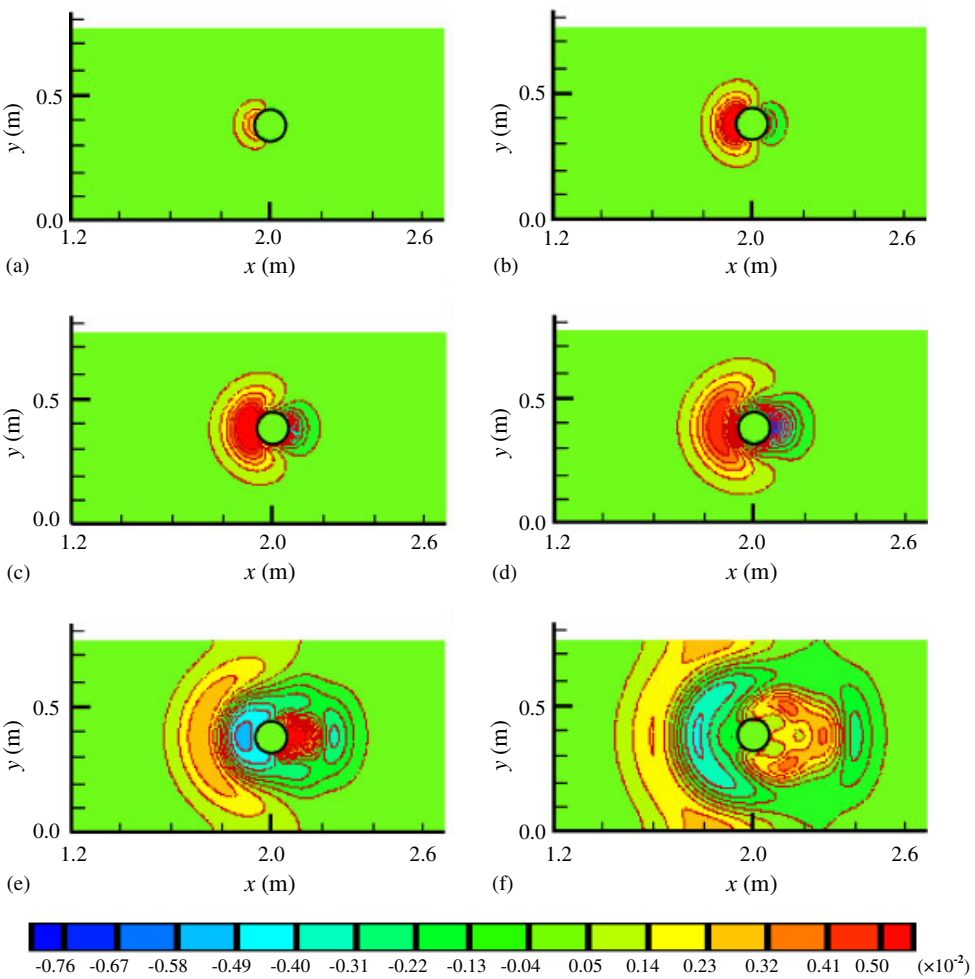

Figure 21. Contours of surface elevation for solitary wave scattered field at various times: (a) $t=1.12\,\mathrm{s}$; (b) $t=1.24\,\mathrm{s}$; (c) $t=1.32\,\mathrm{s}$; (d) $t=1.40\,\mathrm{s}$; (e) $t=1.60\,\mathrm{s}$; and (f) $t=1.80\,\mathrm{s}$.

Figure 25 depicts the time histories of wave elevations at $x/R=-2,-1,0$ and 1 for $h/R=1$ and $H/h=0.4$ and at $x/R=-4,-1,0,1$ for $h/R=3$ and $H/h=0.2$. We can see that the maximum surface elevation always occurs at the front of the cylinder, where $x/R=-1$.

6. CONCLUSIONS

The Boussinesq-type equations derived by Madsen and Sørensen are solved on a Cartesian cut-cell grid using a second-order MUSCL-Hancock Godunov-type finite volume scheme. This numerical model is validated for solitary wave reflection from a vertical wall and for solitary wave reflection and diffraction by a truncated barrier. The model has then been used to simulate solitary wave

DOI: 10.1002/fld

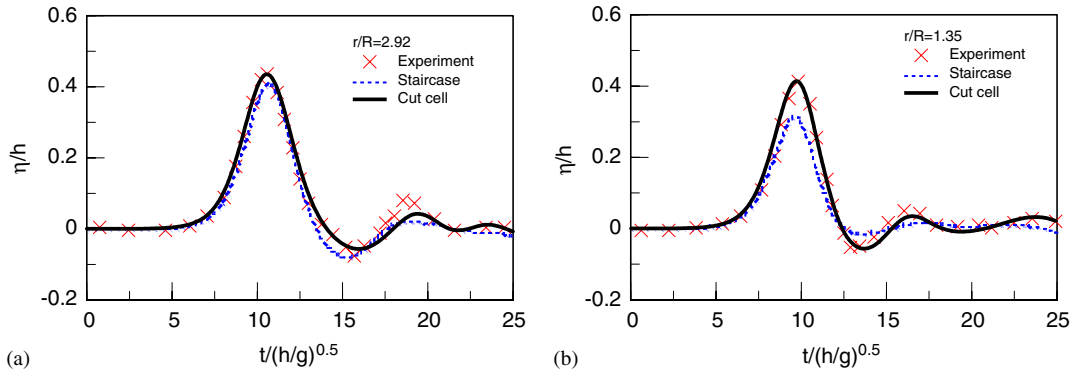

Figure 22. Wave elevation time histories for cut cell and staircase grids: $\theta = 100°$.

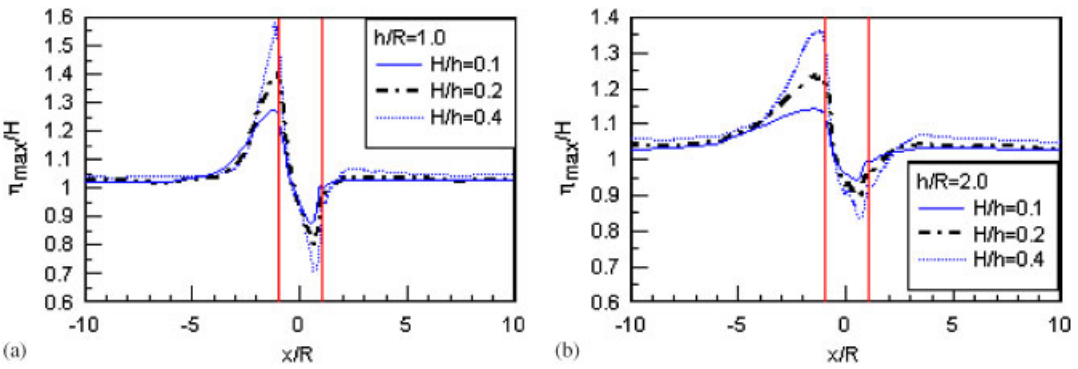

Figure 23. The maximum wave run up along the centreline.

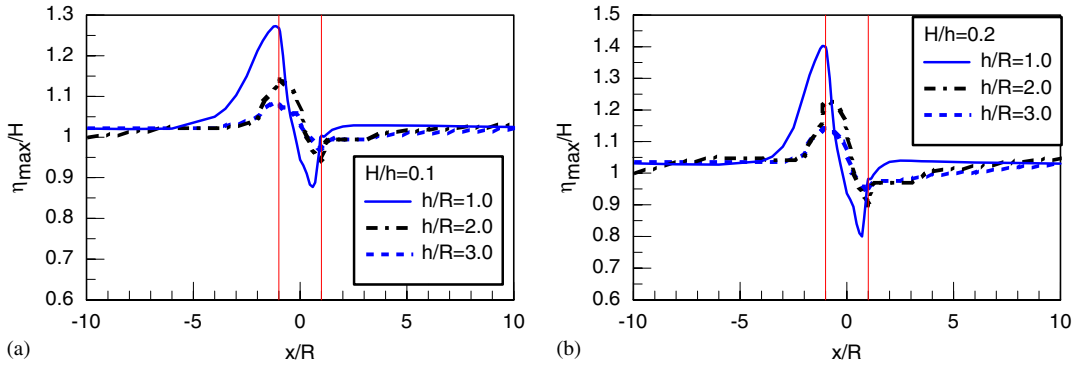

Figure 24. The maximum wave run up along the centreline.

DOI: 10.1002/fld

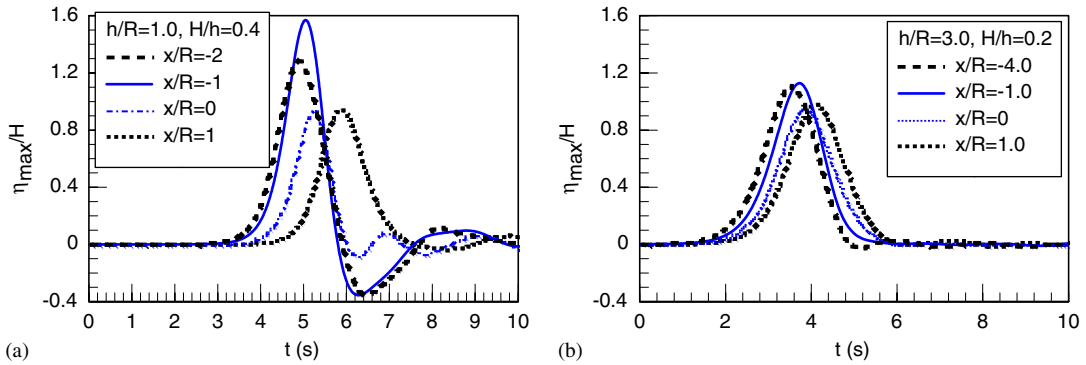

Figure 25. Time histories of maximum free surface elevation at different locations.

interaction with a vertical surface-piercing circular cylinder. The predicted free surface motions and run up at the cylinder are very similar to published results obtained experimentally and from an alternative numerical scheme. The incoming solitary wave impacts against the cylinder causing maximum run up at the front stagnation point, followed by reflected back-scattered waves that travel against the direction of the solitary wave and secondary diffracted waves that propagate behind the cylinder. The scattered wave structure forms a three-ring series of circular waves, which are thought to be due to second-order sum wave components. The cut-cell Boussinesq model is applicable to the phase-resolved simulation of waves and currents interacting with maritime structures with arbitrarily complicated geometry situated in shallow coastal waters where the waves are non-breaking.

ACKNOWLEDGEMENTS

The authors gratefully acknowledge financial support from U.K. Engineering and Physical Science Research Council under EPSRC Grant GR/T07220/01 and GR/T07220/02.

REFERENCES

1. Madsen PA, Sørensen OR. A new form of the Boussinesq equations with improved linear dispersion characteristics—Part 1. *Coastal Engineering* 1992; **15**:371–388.
2. Nwogu O. Alternative form of Boussinesq equations for nearshore wave propagation. *Journal of Waterway*, *Port*, *Coastal*, *Ocean Engineering* (ASCE) 1993; **119**:618–638.
3. Wei G, Kirby JT, Grilli ST, Subramanya R. A fully nonlinear Boussinesq model for surface waves. I. Highly nonlinear, unsteady waves. *Journal of Fluid Mechanics* 1995; **294**:71–92.
4. Chen Q, Madsen PA, Schäffer HA, Basco DR. Wave–current interaction based on an enhanced Boussinesq approach. *Coastal Engineering* 1998; **33**(1):11–39.
5. Shi FY, Robert AD, Kirby JT. A fully nonlinear Boussinesq model in generalized curvilinear coordinates. *Coastal Engineering* 2001; **42**(4):337–358.
6. Fuhrman DR, Bingham HB, Madsen PA. Nonlinear wave–structure interactions with a high-order Boussinesq model. *Coastal Engineering* 2005; **52**(8):655–672.
7. Zerihun YT, Fenton JD. One-dimensional simulation model for steady transcritical free surface flows at short length transitions. *Advances in Water Resources* 2006; **29**(11):1598–1607.
8. Kawahara M, Cheng JY. Finite element method for Boussinesq wave analysis. *International Journal of Computational Fluid Dynamics* 1994; **2**:1–17.

DOI: 10.1002/fld

9. Ambrosi D, Quartapelle L. A Taylor–Galerkin method for simulation of nonlinear-dispersive water waves. *Journal of Computational Physics* 1998; **146**:546–569.
10. Zhao M, Teng B, Cheng L. A new form of generalized Boussinesq equations for varying water depth. *Ocean Engineering* 2004; **31**:2047–2072.
11. Weston BP. A Godunov-type Boussinesq model of extreme wave run-up and overtopping. *D.Phil. Thesis*, University of Oxford, U.K., 2004.
12. Borthwick AGL, Ford M, Weston BP. Solitary wave transformation, breaking and run-up at a beach. *Journal of Maritime Engineering* 2006; **MA0**:1–9.
13. Park JH, Chung TJ, Yun FS. The onset of longitudinal vortex rolls in the thermal entrance region of plane Poiseuille flow heated with a constant heat flux. *International Journal of Heat and Mass Transfer* 2006; **49**(19–20):3708–3716.
14. Causon D, Ingram D, Mingham C, Yang G, Pearson R. Calculation of shallow water flows using a Cartesian cut cell approach. *Advances in Water Resources* 2000; **23**:545–562.
15. Causon DM, Ingram DM, Mingham CG. A Cartesian cut cell method for shallow water flows with moving boundaries. *Advances in Water Resources* 2001; **24**:899–911.
16. Quirk J. An alternative to unstructured grids for computing gas dynamic flows around arbitrarily complex two-dimensional bodies. *Computers and Fluids* 1994; **23**(1):125–142.
17. Yang G, Causon D, Ingram D, Saunders R, Batten P. A Cartesian cut cell method for compressible flows—Part A, Static body problems. *Aeronautical Journal* 1997; **101**(1001):47–56.
18. Yang G, Causon D, Ingram D. Calculation of compressible flows about complex moving geometries using a 3D Cartesian cut cell method. *International Journal of Numerical Methods in Fluids* 2000; **33**:1121–1151.
19. Cieslak S, Khelil SB, Choqiet I, Merlen A. Cut cell strategy for 3D blast wave numerical simulation. *Shock Waves* 2001; **10**(6):421–429.
20. Liang Q, Zang J, Borthwick AGL, Taylor PH. Shallow flow simulation on dynamically adaptive cut cell quadtree grids. *International Journal for Numerical Methods in Fluids* 2007; **53**(12):1777–1799.
21. Tucker P, Pan Z. A Cartesian cut cell method for incompressible viscous flow. *Applied Mathematical Modelling* 2000; **24**:591–606.
22. Mittal R, Udaykumar H, Shyy W. An accurate Cartesian grid method for viscous incompressible flows with complex immersed boundaries. *Journal of Computational Physics* 1999; **156**:209–240.
23. LeVeque R, Shyue K. Two dimensional front tracking based on high resolution wave propagation methods. *Journal of Computational Physics* 1996; **123**:354–368.
24. Ivings M. Wave propagation through gases and liquids. *Ph.D. Thesis*, Department of Computing and Mathematics, Manchester Metropolitan University, 1997.
25. Qian L, Causon DM, Ingram DM, Mingham CG, Zhou JG. A Cartesian cut cell method for incompressible viscous flows. *Proceedings of the European Community on Computational Methods in Applied Science*, *CFD 2001*, Institute of Mathematics and its Applications, Southend-on-Sea, U.K., 2001.
26. Sabersky RH, Acosta AJ, Hauptmann EG. *Fluid Flow* (3rd edn). Macmillan: New York, 1989; 230.
27. Fujihara M, Borthwick AGL. Godunov-type solution of curvilinear shallow-water equations. *Journal of Hydraulic Engineering* (ASCE) 2000; **126**(11):827–836.
28. Sankaranarayanan S, Spaulding ML. A study of the effects of grid non-orthogonality on the solution of shallow water equations in boundary-fitted coordinate systems. *Journal of Computational Physics* 2003; **184**:299–320.
29. Anastasiou K, Chan CT. Solution of the 2D shallow water equations using the finite volume method on unstructured triangular meshes. *International Journal for Numerical Methods in Fluids* 1997; **24**(11):1225–1245.
30. Namin M, Lin B, Falconer RA. Modelling estuarine and coastal flows using an unstructured triangular finite volume algorithm. *Advances in Water Resources* 2004; **27**:1179–1197.
31. Yang G, Causon DM, Ingram DM, Saunders R, Batten P. A cartesian cut cell method for compressible flows. Part A: static body problems. *Aeronautical Journal* 1997; **101**(1002):47–56.
32. Tseng Y-H, Ferziger JH. A ghost-cell immersed boundary method for flow in complex geometry. *Journal of Computational Physics* 2003; **192**:593–623.
33. Rogers BD, Borthwick AGL, Taylor PH. Mathematical balancing of flux gradient and source terms prior to using Roe's approximate Riemann solver. *Journal of Computational Physics* 2003; **192**(2):422–451.
34. VanLeer B. On the relation between the upwind-difference schemes of Godunov, Engquist-Osher and Roe. *SIAM Journal on Scientific and Statistical Computing* 1984; **5**:1–20.
35. Toro EF. *Shock Capturing Methods for Free-surface Shallow Flows*. Wiley: New York, 2001.
36. Tseng YH, Ferziger JH. A ghost-cell immersed boundary method for flow in complex geometry. *Journal of Computational Physics* 2003; **192**:593–623.

DOI: 10.1002/fld

37. Byatt-Smith, JGB, An integral equation for unsteady surface waves and a comment on the Boussinesq equation. *Journal of Fluid Mechanics* 1971; **49**:625–633.
38. Perroud PH. The solitary wave reflection along a straight vertical wall at oblique incidence. *Technical Report Series 99*, Issue 3, Institute of Engineering Research, University of California, Berkeley, CA, 1957.
39. Yates GT, Wang KH. Solitary wave scattering by a vertical cylinder: experimental study. *Proceedings of the Fourth International Offshore and Polar Engineering Conference*, Osaka, vol. 3, 1994; 118–124.
40. Buldakov EV, Eatock Taylor R, Taylor PH. Diffraction of a directionally spread wave group by a cylinder. *Applied Ocean Research* 2003; **25**:301–320.
41. Buldakov EV, Eatock Taylor R, Taylor PH. Local and far-field surface elevation around a vertical cylinder in unidirectional steep wave groups. *Ocean Engineering* 2004; **31**:833–864.

DOI: 10.1002/fld